

Effective Window Function for Lagrangian Halos

Kwan Chuen Chan^{(1,2),*} Ravi K. Sheth⁽³⁾, and Román Scoccimarro⁽⁴⁾

¹ *Département de Physique Théorique and Center for Astroparticle Physics, Université de Genève, 24 quai Ernest Ansermet, CH-1211 Genève 4, Switzerland*

² *Institut de Ciències de l'Espai, IEEC-CSIC, Campus UAB, Carrer de Can Magrans, s/n, 08193 Bellaterra, Barcelona, Spain*

³ *Center for Particle Cosmology, University of Pennsylvania, 209 S. 33rd St., PA 19104, Philadelphia, USA and*

⁴ *Center for Cosmology and Particle Physics, Department of Physics, New York University, NY 10003, New York, USA*

(Dated: December 8, 2024)

The window function for protohalos in Lagrangian space is often assumed to be a tophat in real space. We measure this profile directly and find that it is more extended than a tophat but less extended than a Gaussian; its shape is well-described by rounding the edges of the tophat by convolution with a Gaussian that has a scale length about 5 times smaller. This effective window W_{eff} is particularly simple in Fourier space, and has an analytic form in real space. Together with the excursion set bias parameters, W_{eff} describes the scale-dependence of the Lagrangian halo-matter cross correlation up to $kR_{\text{Lag}} \sim 10$, where R_{Lag} is the Lagrangian size of the protohalo. Moreover, with this W_{eff} , all the spectral moments of the power spectrum are finite. While this simplifies analysis of the excursion set peak model, the predicted mass function which results is significantly lower, and hence appreciably lower than in simulations for halos of mass $\lesssim 10^{14} h^{-1} M_{\odot}$.

I. INTRODUCTION

The abundance and clustering of virialized dark matter halos can be used to constrain cosmological parameters [1, 2]. The most widely studied models for halos in the late time Eulerian field are said to be Lagrangian: one postulates that the physics of Eulerian halo formation may be understood by studying the Lagrangian protohalos. The reason for doing this is that statistics in the Lagrangian space are simpler than in Eulerian space: this is especially true if the initial field is Gaussian. However, defining the proto-halos theoretically becomes a non-trivial task. One has to determine what conditions are required to define a protohalo.

In the excursion set approach [3, 4] the Lagrangian protohalo patches from which halos later form are modeled by requiring that the smoothed dark matter density field satisfy certain constraints. This is also true for more elaborate models based on peaks [5–10], and excursion set peaks [11–14]. The smoothing window is often assumed to be a tophat in real space, based on physical grounds. E.g., the spherical collapse model is explicitly about tophat spherical shells: the evolution of a shell is governed by the mean tophat overdensity within it [15–17]. The tophat assumption has the added simplicity that the tophat profile is maintained during collapse, until the final violent relaxation phase [18].

However, there are scattered hints from previous numerical studies that the Lagrangian shape is more extended than a tophat [19–25]. Moreover, the peaks-based predictions for halo abundance and formation require in-

tegrals (over the initial power spectrum), some of which are ill-defined for a tophat window. To alleviate this problem, it is common to use a Gaussian window instead [5], or to use a tophat when it leads to convergent results and a Gaussian otherwise [e.g. 13, 14, 26]. Finding a better motivated, less ad hoc treatment is desirable.

In these approaches, the window function affects both the predicted abundance of halos, as well as their clustering. On large scales, the clustering of halos is linearly biased with respect to the matter. As measurements and theoretical predictions become more precise, it has become necessary to account for the fact that this bias may be scale dependent. Correctly modeling this scale dependence requires a good understanding of the window function [5, 27]. Thus, both when predicting halo abundances and when modeling halo bias, the shape the window function plays a crucial role. The main goal of the present study is to use numerical simulations to determine this shape.

In Sec. II, we describe real-space estimates of W_{eff} from simulations, and propose a simple analytic parametrization of it. Fourier space estimates are the subject of Sec. II C. After showing that the effective window works for both real space and Fourier space measurements, we use it to predict the mass function of excursion set peaks in Sec. III. We conclude in Sec. IV. Several details are provided in Appendices. Estimating W_{eff} from a clustered field, rather than the initial Lagrangian grid, is the subject of Appendix A. Dependence on how the halos were defined in the first place is studied in Appendix B. The excursion set peak mass function is reviewed and extended to general window functions in Appendix C. Appendix D discusses the question of how W_{eff} can be understood in the context of the spherical collapse model.

*Electronic address: chan@ice.cat

II. LAGRANGIAN WINDOW FUNCTION

Suppose that one has identified halos in the late time Eulerian field. Then, using the initial positions of the particles, one defines the Lagrangian protohalo patch as the region from which each Eulerian halo forms. In Lagrangian models for halos, one postulates that the physics of Eulerian halo formation may be understood by studying the Lagrangian protohalos. The reason for doing this is that statistics in the Lagrangian space are simpler than that in Eulerian space: this is especially true if the initial field is Gaussian. The cost – there is always a price to pay – is the complexity required to define a protohalo in Lagrangian space (the definition is usually relatively simple in Eulerian space). E.g., are protohalos peaks in density? if so on what scale? is density the only variable which matters? etc.

To study the halos in Lagrangian space numerically, we construct the Lagrangian halos as follows. From the Eulerian halos identified at some redshift z , typically $z = 0$ and 0.97 in this paper, we trace back the constituent particles in each halo to the initial redshift z_* . The center of mass of the Lagrangian halo is estimated using the center of mass of the constituent particles in the Lagrangian space.

In this work, we use two sets of simulations in the LasDamas project, Oriana and Carmen, respectively. In both simulation sets, the same flat Λ CDM model with the cosmological parameters, $\Omega_m = 0.25$, $\Omega_\Lambda = 0.75$ and $\sigma_8 = 0.8$ are adopted. The transfer function is taken from CMBFAST [28]. The initial conditions are Gaussian with spectral index $n_s = 1$. The initial particle displacement fields are set using 2LPT [29] at $z_* = 49$, after which the particles are evolved using the public code Gadget2 [30]. In the Oriana simulations, there are 1280^3 particles in a cubic box of size $2400 h^{-1}\text{Mpc}$, and 1120^3 particles in a box of size $1000 h^{-1}\text{Mpc}$ in the Carmen simulations. Thus, in the Oriana and Carmen simulations, each particle carries a mass of 4.57×10^{11} and $4.94 \times 10^{10} h^{-1} M_\odot$ respectively. Our results are averaged over 5 realizations for Oriana, and 7 for Carmen. In each simulation, the Eulerian halos are identified using the Friends-Of-Friends algorithm [31, hereafter FOF] with linking length $b = 0.156$. We show results with $b = 0.2$ in Appendix B. The halo catalogs are constructed at $z = 0.97$ and 0 . To resolve the halo profiles well, we consider halos with at least 60 particles. We bin the halos into narrow mass bins of width $\Delta \ln M = 0.157$.

A. The Lagrangian window in real space

There are several requirements that we expect the window function W to satisfy. To define a halo in Lagrangian space, we expect it to be compact and reasonably well lo-

calized in real space. We also require $W(\mathbf{x}) \geq 0$ and

$$\int d\mathbf{x} W(\mathbf{x}) = 1. \quad (1)$$

Although we know that halos, and the protohalo patches from which they formed, are not really spherical [e.g. 22, 32], we will assume, for simplicity, that W is spherically symmetric. With these minimal conditions, we now describe how we reconstruct the effective window function from the Lagrangian halo profile.

Consider a protohalo centered at the origin. The total number of particles in this halo, N , is given by

$$N = \int d\mathbf{x} n_h(\mathbf{x}) = \int dr 4\pi r^2 p_h(r) n_m(r), \quad (2)$$

where n_m is the number density of dark matter particles, p_h is the probability that a dark matter particle at distance r from the protohalo center is part of the protohalo.

Even when the Lagrangian halo profile is not tophat, it is convenient to define the Lagrangian radius R_{Lag} as

$$N = \frac{4\pi}{3} \bar{n}_m R_{\text{Lag}}^3, \quad (3)$$

where \bar{n}_m is the mean density of dark matter particles. Then Eq. 1 indicates that we should define

$$W(r) \equiv \frac{3 p_h(r)}{4\pi R_{\text{Lag}}^3} \frac{n_m(r)}{\bar{n}_m}. \quad (4)$$

We estimate $p_h(r)$ for each protohalo from the ratio $n_h(r)/n_m(r)$, where $n_h(r)$ is the number density of particles belonging to the Lagrangian halo. The results are shown in Fig. 1. To compute $n_h(r)$, for each Lagrangian halo, we bin all the particles at the grid position belonging to the Lagrangian halo into spherical shells about the center of mass of the halo, and we then compute the number density of the shells. The spherically averaged number density is further averaged over all the halos in the same mass bin. We carry out the same procedure for all the particles around the halo center to compute $n_m(r)$. In both cases, we use the particles traced back to the initial grid points, and not the 2LPT displaced positions. This lets us replace n_m with \bar{n}_m in Eq. 2.

Fig. 1 shows the measurements from both Carmen and Oriana with Lagrangian protohalos obtained from Eulerian halos at $z = 0.97$ and 0 respectively. The results from $z = 0.97$ and $z = 0$ are very similar. To absorb most of the mass dependence, the radius is normalized with respect to R_{Lag} . We find that in this normalized variable, the results from halos spanning three orders of magnitude in mass follow a very similar profile. However, there is remains a small residual mass dependence: the less massive halos are slightly more diffuse than the more massive ones.

Fig. 1 shows that the profile drops sharply at $r/R_{\text{Lag}} \sim 1$, but it is smoother than a tophat and more localized than a Gaussian. This agrees with Fig. 3 of [20]. Even

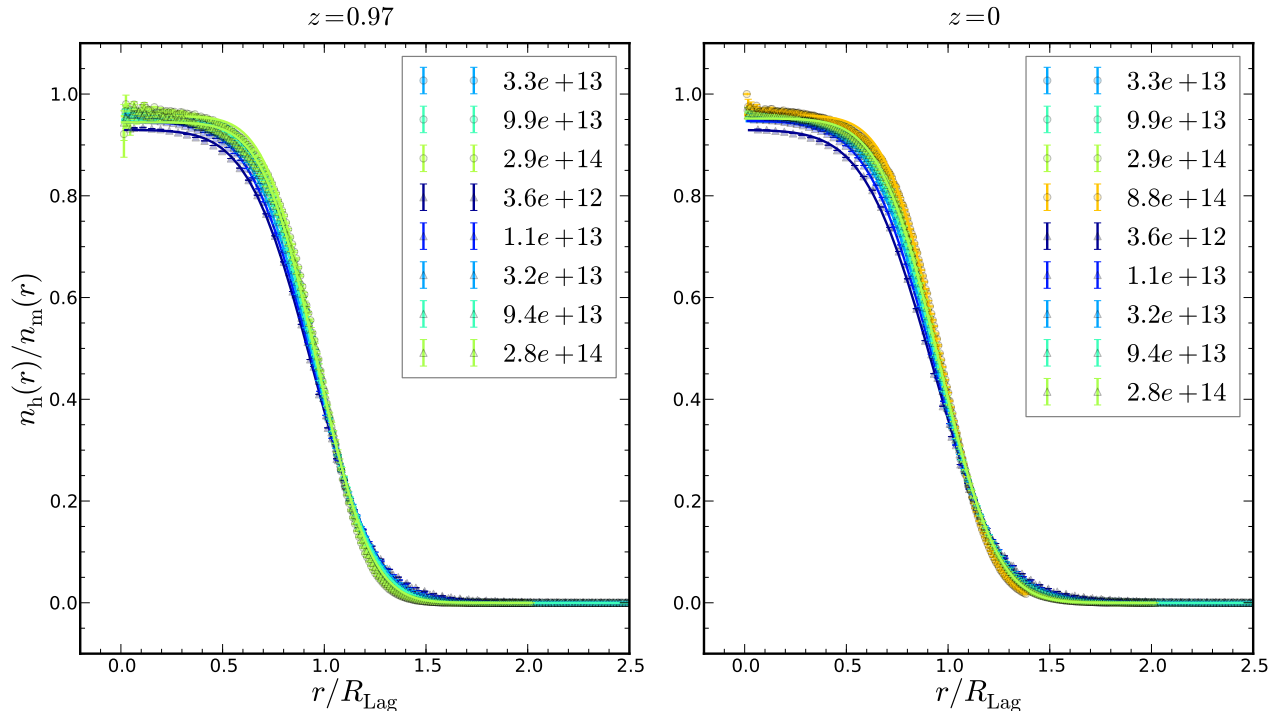


FIG. 1: The estimator n_h/n_m for p_h in Oriana (circles) and Carmen (triangles) for the range of halo masses shown in the legend (in units of $h^{-1}M_\odot$). Solid lines, same color as the data points, show the result of fitting Eq. 7 to the data; in all cases the fit is good.

at $r/R_{\text{Lag}} \lesssim 0.5$, p_h is still a few per cent less than 1. Evidently, a small fraction of the dark matter particles which start out close to the center of mass of the protohalo are not incorporated into the final Eulerian halo. The protohalo may consist of more than one lump. If we use only the main lump in the Lagrangian halo as in [22], the resultant p_h near the center would be closer to unity.

B. Analytic model for the Lagrangian window

Consider a tophat of radius R_{Lag} centered on a protohalo patch. There are at least two reasons why we expect W to differ from this tophat. First, the protohalos are not spherical, so assuming spherical symmetry can make $p \neq 1$. [32] show that this is a small effect. In addition, particles within R_{Lag} having velocities larger than the escape speed will escape (i.e. more beyond R_{Lag}); others which were initially beyond R_{Lag} may have had velocities which brought them closer. Both types of particles will smear out the sharp edge. This motivates us to consider a composite window consisting of a tophat smoothed by a Gaussian. In principle, the mean and width of this Gaussian depend on distance from the protohalo center. In what follows, we ignore this subtlety. I.e., we define

$$W_{\text{eff}}(kR_{\text{Lag}}) \equiv W_{\text{TH}}(kR_{\text{Lag}}) W_{\text{G}}\left(\frac{\sqrt{f}kR_{\text{Lag}}}{5}\right), \quad (5)$$

where

$$W_{\text{TH}}(x) \equiv \frac{3}{x^3}(\sin x - x \cos x) \text{ and } W_{\text{G}}(x) \equiv e^{-x^2/2}. \quad (6)$$

We will see later on that the scale of the Gaussian window is approximately the same as the Eulerian scale; it is about 1/5 of the size of the tophat (R_{Lag}). The parameter f quantifies how the scale of W_{G} differs from $R_{\text{Lag}}/5$. (Of course, had we assumed a smoothing window other than a Gaussian, the associated scale would have been slightly different.)

One of the virtues of this functional form is that its inverse Fourier transform is analytic. The effective window in real space is

$$W_{\text{eff}}(r) = \frac{3}{4\pi R_{\text{Lag}}^3} \left\{ \frac{\sqrt{f}}{5\sqrt{2\pi}} \frac{e^{-x_+^2} - e^{-x_-^2}}{x} + \frac{\text{erf}(x_+)}{2} - \frac{\text{erf}(|x_-|)}{2x} \left[\frac{x_-}{|x_-|} + |x-1| \right] \right\}, \quad (7)$$

where

$$x \equiv \frac{r}{R_{\text{Lag}}}, \quad x_+ \equiv \frac{5(x+1)}{\sqrt{2f}}, \quad x_- \equiv \frac{5(x-1)}{\sqrt{2f}}. \quad (8)$$

When fitting to the data in Fig. 1 we replace $R_{\text{Lag}} \rightarrow \rho R_{\text{Lag}}$, and allow ρ and f to vary. In addition, we multiply the expression above by an overall amplitude A ,

which we also allow to vary. Fig. 2 shows the best fit parameters. We expect ρ and A to be close to 1 for all masses, and Fig. 2 shows that this is indeed the case. On the other hand, f is a stronger function of halo mass: it is larger than unity at small masses, and decreases at large masses. This mass-dependence is different for the two redshifts we have studied, but the redshift dependence is reduced significantly if we express the masses and redshifts in terms of the scaled variable $\nu \equiv \delta_c(z)/\sigma_0(M)$, where $\delta_c(z)$ is the time-dependent spherical collapse threshold and $\sigma_0(M)$ is defined in Eq. 13. When this is done, $f \sim 1.50$ at $\nu \sim 1.5$, but is smaller than unity at $\nu \gg 1$, passing through unity at $\nu \sim 4$.

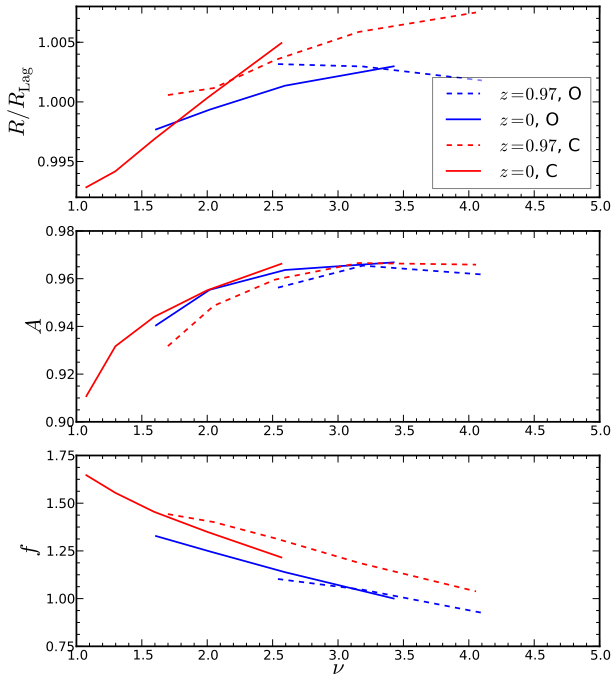


FIG. 2: The best-fit parameters ρ , A and f for the Lagrangian protohalo profiles. The best fit to the data from Oriana (blue) and Carmen (red) at $z = 0.97$ (dashed) and 0 (solid) are shown.

C. Fourier space estimate of the window

We now focus on the cross correlation between the protohalo centers and the dark matter; we will not consider the auto-correlation. This halo-matter cross-correlation function is related to the auto-correlation of the dark matter by a multiplicative (possibly scale dependent) linear bias factor [33]. In Fourier space, the cross power spectrum between the Lagrangian halo density contrast, δ_h , and that of the dark matter at the initial time, δ_m , is

$$\langle \delta_h(\mathbf{k}_1) \delta_m(\mathbf{k}_2) \rangle = (2\pi)^3 P_c(k_1) \delta_D(\mathbf{k}_{12}), \quad (9)$$

where δ_D is the Dirac delta function. Similarly, the Lagrangian matter power spectrum is defined as

$$\langle \delta_m(\mathbf{k}_1) \delta_m(\mathbf{k}_2) \rangle = (2\pi)^3 P_m(k_1) \delta_D(\mathbf{k}_{12}). \quad (10)$$

Using P_c and P_m , we can define the Lagrangian cross bias parameter

$$b_c^L(k, z) = \frac{D(z_*)}{D(0)} \left[\frac{P_c(k)}{P_m(k)} - 1 \right], \quad (11)$$

where we extrapolate the Lagrangian bias parameter to $z = 0$ using the linear growth factor D . We have included the term -1 because of finite initial redshift of the simulation, see e.g. [34].

Fig. 3 shows our measurements of b_c^L (the right hand side of Eq. 11) for the protohalo patches of halos identified at $z = 0.97$ (left) and 0 (right) in both Oriana and Carmen for a range of halo masses. Plotting this quantity versus kR_{Lag} rather than k alone removes some of the dependence on mass. For $kR_{\text{Lag}} \lesssim 1$, this quantity approaches a (mass-dependent) constant; it rises to a maximum at $kR_{\text{Lag}} \sim 1$, after which it drops sharply and oscillates with diminishing amplitude as kR_{Lag} increases.

In the excursion set approach, the Lagrangian cross bias b_c^L is [27]

$$b_{\text{eff}}(k) = \left[b_{10} + 2b_{01} \frac{d \ln W_{\text{eff}}(k)}{d \ln s_0} \right] W_{\text{eff}}(k) \quad (12)$$

where

$$s_j \equiv \sigma_j^2 = \int \frac{dk}{k} \frac{4\pi k^3}{(2\pi)^3} k^{2j} P_m(k, 0) W_{\text{eff}}^2(kR), \quad (13)$$

with $P_m(k, 0)$ is the initial dark matter power spectrum extrapolated using linear theory to $z = 0$, and b_{10} and b_{01} are dimensionless bias parameters whose numerical values depend on protohalo mass (i.e. on R_{Lag}). Note that with W_{eff} all the spectral moments of the power spectrum are finite. Typically, $W_{\text{eff}} \rightarrow 1$ as $k \rightarrow 0$. In this limit $b_{\text{eff}}(k) \rightarrow b_{10}$, so b_{10} can be estimated reliably with little knowledge of the window. However, the expression above shows that, to measure the bias parameter b_{01} associated with scale dependent bias, one must model the window function accurately.

A Gaussian smoothing window has long been a popular choice [e.g. 21, 24]. However, the obvious oscillations at large kR_{Lag} in Fig. 3 rule this out as a viable model. On the other hand, the amplitude of oscillations we measure is damped relative to a tophat. This suggests that our W_{eff} , a Gaussian smoothed tophat, may be able to provide a good description of our Fourier space measurements. To test this, we insert Eq. 5 into Eq. 12, set $f = 1$ and treat b_{10} , b_{01} and R as free parameters when fitting b_{eff} to our measurements. To simplify the fitting, we first determine b_{10} by fitting to $kR_{\text{Lag}} \leq 0.15$. We then keep this value of b_{10} fixed and fit b_{01} and R using the full range of kR_{Lag} .

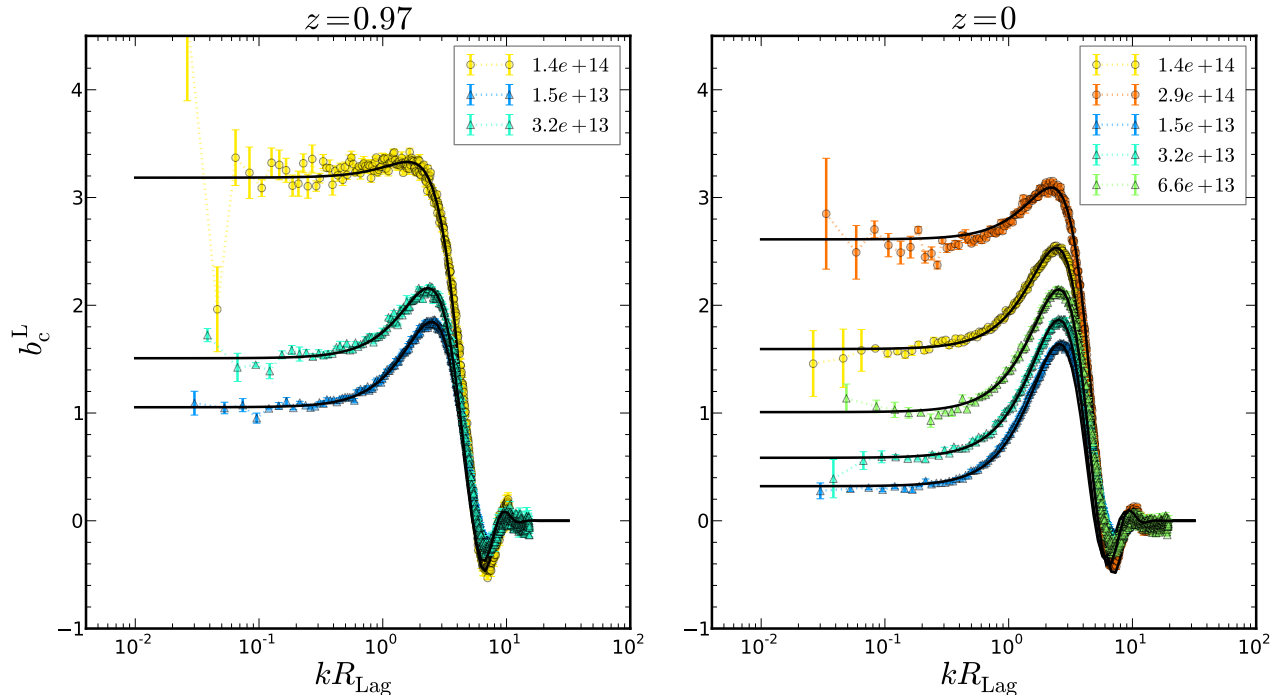


FIG. 3: The Lagrangian cross bias parameter b_c^L for the Lagrangian protohalos of Eulerian halos at $z = 0.97$ (left) and $z = 0$ (right) in the Oriana (circle) and Carmen (triangle) simulations, for a range of halo masses (legend, in units of $h^{-1}M_\odot$). Solid black curves show the result of fitting Eq. 12 to these measurements.

The solid curves in Fig. 3 show our best fits. Overall, b_{eff} fits our measurements very well. As the focus of this paper is W_{eff} , we shall not describe the best-fit bias parameters b_{10} and b_{01} in detail here; we discuss their implications elsewhere [35]. However, we note that the best-fit R is roughly within 10% of R_{Lag} . This means that both the halo profile in real space and the cross bias parameter in Fourier space require the same W_{eff} . This is an important consistency check of the model.

III. EXCURSION SET PEAK MASS FUNCTION USING THE EFFECTIVE WINDOW

Unlike the excursion set approach [3], the peak model [5] only takes one particular scale into account. The excursion set approach assumes that the halo abundance can be obtained by averaging over random points, while in peak model, the average is taken over the peak positions only. Refs. [11–13] incorporated the first crossing constraint, which is crucial in the excursion set formalism, into the peak model. Hence the resultant model is dubbed excursion set peak (ESP). The spectral moments s_j of Eq. (13) play an important role in the ESP approach; they depend on the window function. In this section we check how the ESP mass function changes when the effective window is used. In Appendix C, we review the derivations of the ESP mass function in detail.

In particular, in [11–13] the Gaussian window function was assumed, we will generalize the ESP mass function to arbitrary window function.

We shall follow the prescription in [13], in which the mass dependence of the barrier and the scatter around the barrier are important ingredients. The barrier is modeled by

$$B(s_0) = \delta_c + \epsilon\sqrt{s_0}, \quad (14)$$

where the square-root model is to describe the scale-dependence of the barrier and ϵ controls the scatter around the barrier (Note that our ϵ is β in [13]). The ESP multiplicity function f_{esp} is obtained by averaging over the scatter

$$f_{\text{esp}}(\nu) = \int d\epsilon f_{\text{esp}}(\nu|\epsilon)p(\epsilon). \quad (15)$$

Ref. [13] followed [36] to use log-normal distribution for $p(\epsilon)$ with $\langle\epsilon\rangle = 0.5$ and $\text{Var}(\epsilon) = 0.25$. As our aim here is to check the effect of the window function, we shall do the same.

For the Gaussian window, the conditional ESP multiplicity function is given by [13]

$$f_{\text{esp}}^G(\nu|\epsilon) = \frac{V}{V_*} \frac{e^{-(\nu+\epsilon)^2/2}}{\sqrt{2\pi}} \frac{1}{\gamma\nu} \int_{\epsilon\gamma}^{\infty} dx (x - \epsilon\gamma) \times f(x)p_G(x;\nu\gamma, 1 - \gamma^2), \quad (16)$$

where γ is the correlation coefficient defined in Eq. C22. The explicit form of $f(x)$ is given in Eq. C43 and the volumes V and V_* are defined in Eq. C46. Note that compare to [13] we have neglected the shift in mean of p_G due to the scatter, and we have checked that its effects are small.

We derive the ESP mass function for arbitrary window function in Appendix C. The final f_{esp} can be written as

$$f_{\text{esp}}(\nu|\epsilon) = \frac{V}{V_*} \frac{e^{-(\nu+\epsilon)^2/2}}{\sqrt{2\pi}} \frac{1}{\alpha\nu} E(\nu, \alpha, \beta, \gamma), \quad (17)$$

where E is given by Eq. C50 and the results depend on additional cross correlation coefficients α and β (Eq. C20 and C21). When a Gaussian window is used, α is the same as γ . The function E can be regarded as a generalization of the integral in Eq. 16.

From f_{esp} , we can derive the halo mass function as usual

$$\frac{dn}{d \ln M} = \frac{\rho_m}{M} \frac{d \ln \nu}{d \ln M} \nu f_{\text{esp}}(\nu). \quad (18)$$

The window function dependence comes from the spectral moments and also the precise form of f_{esp} . In particular, the mapping between mass and the peak significance ν is modified. In Fig. 4, we plot the ratio between ν obtained from the effective window and the tophat window as a function of mass. We assume $z = 0$ in this plot. Because of stronger damping in the effective window, s_0 is reduced and hence ν is increased compared to when a tophat is used. However, the Jacobian $d \ln \nu / d \ln M$ is almost unchanged.

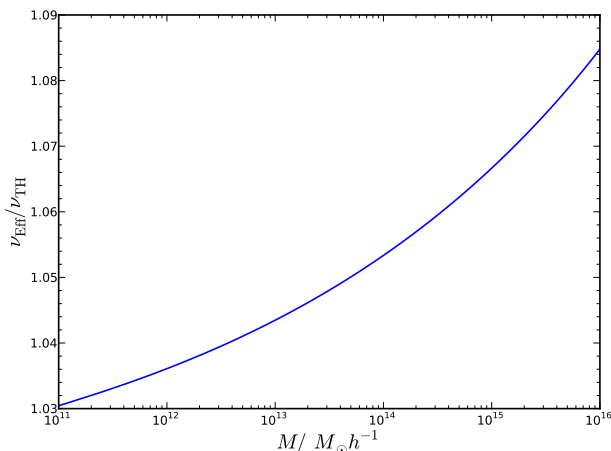


FIG. 4: Dependence of the ratio between ν for the effective and tophat windows on mass.

We shall consider three ways of estimating f_{esp} . In the first, we compute f_{esp}^G (Eq. 16) following [13]: i.e., we use two tophats for s_0 , a tophat and a Gaussian for s_1 , and two Gaussians for s_2 , with the scale of the Gaussian

$$R_G \equiv \frac{R_{\text{Lag}}}{\sqrt{5}}. \quad (19)$$

This relation comes from matching the k^2 coefficient of the tophat and Gaussian window functions in Fourier space. While it differs from the matching advocated by [13] the end result is very similar. We use W_{mix} to refer loosely to this prescription.

In the second case, we keep the same dependence of f_{esp}^G on the moments s_j , but the s_j are computed using W_{eff} only. We refer to this as the “partial W_{eff} ” method. For the third, which we call “full W_{eff} ”, we use f_{esp} of Eq. (17) with the s_j computed using W_{eff} . Comparison of these three prescriptions allows us to see if the spectral moments or the functional form of f_{esp} contribute most significantly.

Fig. 5 shows $\nu f_{\text{esp}}(\nu)$ at $z = 0$ for the three different methods. At low masses, $M \sim 10^{12} h^{-1} M_\odot$, νf_{esp} obtained from W_{eff} is lower than that from W_{mix} by about a factor of 2. The full W_{eff} result is even lower than the partial W_{eff} case. For larger masses, $M \gtrsim 10^{15} h^{-1} M_\odot$, the difference between W_{mix} and the full W_{eff} becomes quite small. The main difference between the mixed and effective windows comes from the factor $(V/V_*)/\gamma$ (or $V/V_*/\alpha$ for full W_{eff}) as it is computed with the spectral moments. For example, we find that at $M = 2 \times 10^{13} h^{-1} M_\odot$, compared to the value obtained from the mixed window, the partial W_{eff} result is about 0.56 of the mixed window value and 0.62 of the mixed window value for the full W_{eff} case. The overall mass dependence of this factor is relatively weak. Thus the mass dependence we see in Fig. 5 mainly comes from the difference between the integral in Eq. 16 and E in Eq. (17).

In [13], the ESP mass function using W_{mix} was shown to lie within 5% of the numerical results over the mass range from $10^{11} - 2 \times 10^{14} h^{-1} M_\odot$ (or from $0.6 \leq \nu \leq 2.2$). However Fig. 5 suggests that when W_{eff} is used, νf_{esp} is significantly lower than the one obtained from W_{mix} in the most relevant mass range 10^{11} to $10^{14} h^{-1} M_\odot$.

Refs. [37, 38] tested how well the Lagrangian halos match peaks in the initial conditions using N -body simulations. They found that the halos with mass $M \gtrsim 10^{13} h^{-1} M_\odot$ match peaks with similar mass well, but the matching deteriorates as the mass decreases. The peak model generally is accurate only in the high peak limit, for example for massive halos. Our Fig. 5 qualitatively agrees with their findings, although the deviation from the numerical results expected from Fig. 5 is somewhat larger than that in [38]. Our finding that the ESP mass function is lower than the numerical results for halos of mass $\lesssim 10^{14} h^{-1} M_\odot$ may imply that only some of the low to medium mass halos are directly associated with peaks in the primordial field. Alternatively, perhaps one must apply a more general collapse scenario for these halos, as suggested in [38].

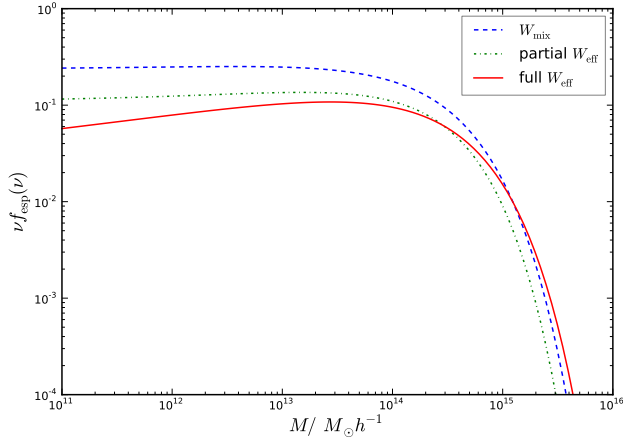


FIG. 5: $\nu f_{\text{esp}}(\nu)$ as a function of mass obtained with different prescriptions: $\nu_{\text{TH}} f_{\text{esp}}^{\text{G}}$ with moments computed using mixed windows (dashed, blue), $\nu_{\text{Eff}} f_{\text{esp}}^{\text{G}}$ with moments computed using the effective window (dotted-dashed, green), and full $\nu_{\text{Eff}} f_{\text{esp}}$ with moments obtained with the effective window (solid, red).

IV. CONCLUSIONS

It is often assumed that the profile of the Lagrangian halos is given by a tophat window function. However, other than being a convenient approximation in the context of the spherical collapse model, there is no fundamental reason why the Lagrangian halo profile should be a tophat. In this paper, we study the profile of the Lagrangian halo using numerical simulations.

The tophat assumption is of course an idealization. Realistically, we expect some particles within the Lagrangian patch of the halo with sufficiently high escape velocity will fly out of it, while others will fall in. Thus we expect that the Lagrangian halo profile will be more extended than a tophat. We measure the spherical profile of the Lagrangian halos by stacking halos together. Indeed the Lagrangian halo profile in real space is more extended than a tophat but less diffuse than a Gaussian. In particular, on average there is still a few per cents of the total particles near the center of mass of the Lagrangian halo do not make it into the final Eulerian halos. We find that the Lagrangian halo window function can be modeled by a product of a tophat and a Gaussian in Fourier space. We also provide an analytic functional form in real space. Thus the modification needed compared to the usual tophat assumption is little.

In Fourier space, the effective bias parameter obtained from the cross power spectrum contains both bias parameters and the window function. Theories such as the peak model can give precise prediction for the scale-dependent bias. The window function contributes additional scale-dependence although its precise form is not constrained by the theory. To distinguish the scale-dependence due to

the bias parameters, the window function must be modeled accurately as well. We find that using the effective window function together with the bias functional form suggested by the excursion set theory, we are able to fit the data well up to $kR_{\text{Lag}} \sim 10$. It is important to note that we find that the same window function is required to fit the Lagrangian halo profile in real space and the cross power spectrum in Fourier space. This is an important self-consistency check.

In models predicting the clustering of the Lagrangian halos, such as the peak model, various spectral moments are required. The tophat window is often used for s_0 , while for higher order moments a Gaussian window is used because the tophat window leads to divergences. However, as we find that the effective window is required to fit the cross bias parameter, we should use the effective window function to compute the moments for self-consistency. The effective window function is more localized in real space than Gaussian, and yet it gives all the convergent spectral moments thanks to its Gaussian component. Thus the effective window offers a unified treatment for all the moments.

We check the ESP mass function when the effective window function is used. We find that the resultant mass function is significantly lower than that from the mixed window approach for halos of mass $\lesssim 10^{14} h^{-1} M_{\odot}$. As previously it was shown that when the mixed window was used, the resultant mass function agrees with simulation results very well, we conclude that when the effective window function is used the results will be significantly lower than the numerical ones. Because the peak model is generally accurate when the high peak limit applies, such as for the massive halos, we can interpret the deficit of the ESP mass function compared to simulation results as that only part of the low mass halos can arise from peaks.

With an accurate effective window function in hand, we are able to measure the scale-dependent bias parameters accurately. We present the details of the measurement of the bias parameters and explore the relations among them elsewhere [35]. In particular we check the so-called consistency relations [13, 27] that these bias parameters should satisfy.

Acknowledgment

We thank Vincent Desjacques and Aseem Paranjape for comments on the draft and the LasDamas project¹ for the simulations used in this work. The simulations were run using a Teragrid allocation and some RPI and NYU computing resources were also used. KCC thanks the hospitality of the ICTP in Trieste and the theory group of CERN, where part of the work was done. KCC

¹ <http://lss.phy.vanderbilt.edu/lasdamas>

acknowledges support from the Swiss National Science Foundation.

Appendix A: Estimating the Lagrangian window from the displaced field

We now discuss a method which uses the displaced particles to estimate p_h . As we mentioned in Sec. II A, in this case we cannot replace n_m by \bar{n}_m . Due to the presence of the halo at the origin, we must set

$$n_m(r) = \bar{n}_m[1 + \xi_c(r)], \quad (\text{A1})$$

where ξ_c is the cross correlation function between halo and matter. We can either measure ξ_c directly or model it. To model ξ_c we use the bias model Eq. 12 given together with the bias parameters computed from the peak model [13] to obtain the cross power spectrum. Then ξ_c follows after an inverse Fourier transform. As in this paper, we focus on the window function, we will present the details of the model and the comparison with numerical measurements elsewhere [35]. We find that the model we adopted describes the simulation data well. Hence we will use ξ_c obtained from theory here. In Fig. 6, we compare the measurement n_h^d/\bar{n}_m and $n_h^d/\bar{n}_m/(1 + \xi_c)$, where the superscript d in n_h^d emphasizes that it is estimated using the displaced particle distribution. We have used the Lagrangian halos at $z = 0$ from the Carmen simulation in this plot. The clustering correction is mainly important for $r \lesssim R_{\text{Lag}}$, while for larger r , $\xi_c \ll 1$. Due to the clustering enhancement, n_h^d/\bar{n}_m exceeds 1 for $r/R_{\text{Lag}} \lesssim 0.5$. After the correction, we find that the results agree with those from the method described in the main text very well (right panel of Fig. 1). This method is interesting in its own right: That we are able to correct for the clustering effect is a non-trivial consistency check of our approach.

Appendix B: The linking length dependence of the Lagrangian halo profile

In the main text we have presented the results using halos obtained with linking length $b = 0.156$. In this section, we study the linking length dependence of the Lagrangian halo profile by comparing the halo profile obtained with $b = 0.156$ and $b = 0.2$.

In Fig. 7, we compare the Lagrangian halo profiles obtained with the two different linking lengths. In this plot, we have used Lagrangian halos obtained from Carmen simulation at $z = 0$. We have considered a narrow mass group whose mean mass is $9.4 \times 10^{13} h^{-1} M_\odot$. We find that with larger b the Lagrangian halo profile becomes more compact. In particular, the fraction of the particles near the halo center that are incorporated into the final Eulerian halos is enhanced when larger b is used. However, one should bear in mind that suppose a halo is identified with $b = 0.156$ to be of certain mass, when

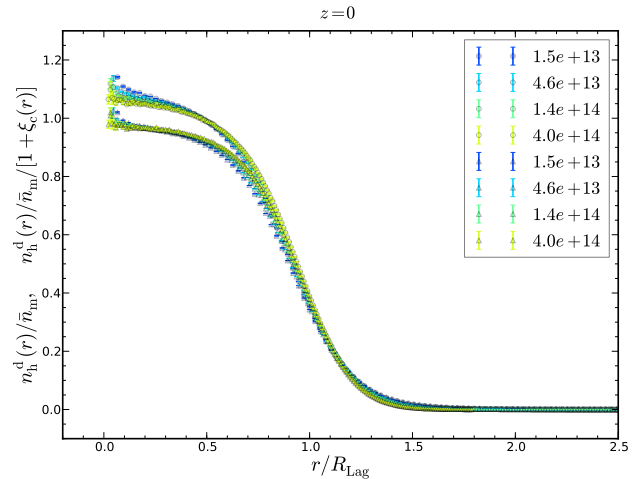


FIG. 6: The ratio n_h^d/\bar{n}_m obtained using displaced particles at the initial redshift $z_* = 49$ (circles, the upper set of curves) and the one with clustering effect corrected $n_h/\bar{n}_m/(1 + \xi_c)$ (triangles, the lower set). The Lagrangian halos at $z = 0$ from Carmen simulation are used.

$b = 0.2$ is applied, this halo will be classified to be a halo of larger mass. Thus if we compare the halos obtained with $b = 0.156$ and $b = 0.2$ in a narrow mass range, we are in fact comparing different objects.

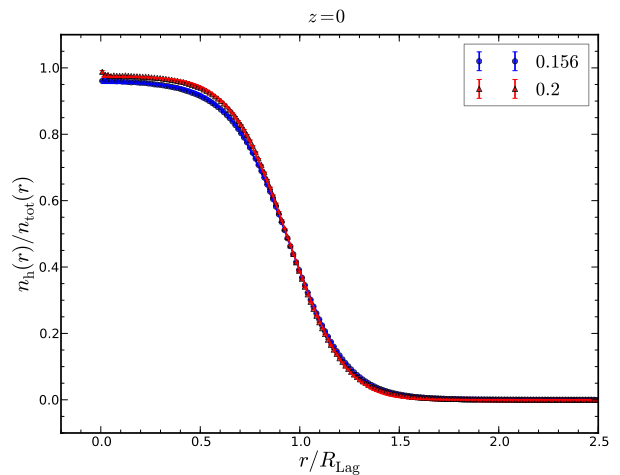


FIG. 7: The Lagrangian halo profile obtained from Eulerian halos with $b = 0.156$ (blue circles) and 0.2 (red triangles) respectively. In this plot, both groups are in the same mass range, whose mean mass is $9.4 \times 10^{13} h^{-1} M_\odot$.

We now select the samples such that we are comparing the same halos. To make sure we are comparing the same object, we search the halo catalog in the $b = 0.2$ group and select the ones that match the center of mass positions in the $b = 0.156$ group. For the mass group whose mean mass $9.6 \times 10^{13} h^{-1} M_\odot$ in the $b = 0.156$ catalog, we find that the corresponding group in $b =$

0.2 has a mean mass increased by about 20% to $1.1 \times 10^{14} h^{-1} M_\odot$. In Fig. 8, we compare the profiles of these two groups. Note that R_{Lag} is computed using the mean mass of the corresponding group. The results are very similar to those in Fig. 7. Increase in b results in a more compact halo group.

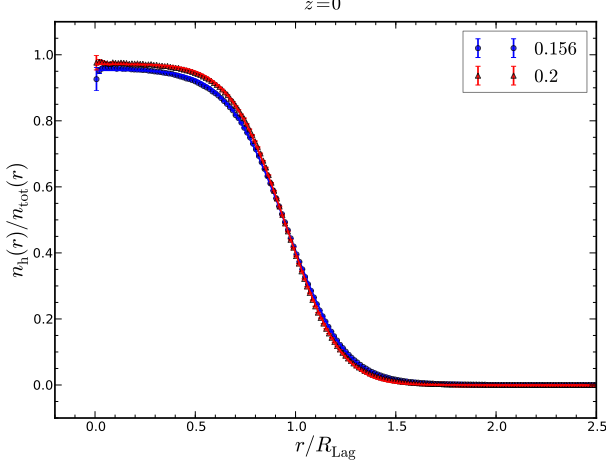


FIG. 8: Similar to Fig. 7 except in this plot, the samples are chosen such that the halos in the $b = 0.156$ group are the same as those in the $b = 0.2$ group. For the $b = 0.156$ group, the mean mass is $9.6 \times 10^{13} h^{-1} M_\odot$, while the mean mass of the $b = 0.2$ group is $1.1 \times 10^{14} h^{-1} M_\odot$.

Appendix C: The excursion set peak mass function with general window function

Excursion set peak (ESP) mass function was derived in [11–13]. However, Gaussian window is assumed in the derivation in those references. In this section, we shall review the derivation of ESP mass function, but we will also generalize it to the case with general window function. The computations below follow Appendix A of [5] closely.

In peak theory, we are interested in the correlation between the density contrast δ , its spatial derivatives $\eta_i = \partial_i \delta$, and its second derivatives $\zeta_{ij} = \partial_{ij} \delta$. We will also impose the first crossing constraint on the peaks. To do so we need an extra variable μ [4, 11, 12]

$$\mu = \frac{d\delta}{ds_0}. \quad (\text{C1})$$

We will assume that the field is Gaussian, thus the statistics of the field is fully encoded in the covariance matrix. The field is smoothed with a general window function W , although most of the time we will keep it implicit.

Suppose we assume the vector to be $\mathbf{V} = (\delta, \mu, \zeta_{11}, \zeta_{22}, \zeta_{33}, \zeta_{12}, \zeta_{23}, \zeta_{13}, \eta_1, \eta_2, \eta_3)^T$, then the ele-

ments of the covariance matrix $M = \langle \mathbf{V} \mathbf{V}^T \rangle$ are

$$\langle \delta^2 \rangle = s_0, \quad (\text{C2})$$

$$\langle \delta \mu \rangle = \frac{1}{2}, \quad (\text{C3})$$

$$\langle \delta \eta_i \rangle = 0, \quad (\text{C4})$$

$$\langle \delta \zeta_{ij} \rangle = -\frac{1}{3} s_1 \delta_{ij}, \quad (\text{C5})$$

$$\langle \mu^2 \rangle = \sigma_\mu^2 = \int \frac{d^3 k}{(2\pi)^3} P(k) \left(\frac{dW}{ds_0} \right)^2, \quad (\text{C6})$$

$$\langle \mu \eta_i \rangle = 0, \quad (\text{C7})$$

$$\langle \mu \zeta_{ij} \rangle = -\frac{1}{6} \delta_{ij} \frac{ds_1}{ds_0}, \quad (\text{C8})$$

$$\langle \eta_i \eta_j \rangle = \frac{1}{3} s_1 \delta_{ij}, \quad (\text{C9})$$

$$\langle \eta_i \zeta_{jk} \rangle = 0, \quad (\text{C10})$$

$$\langle \zeta_{ij} \zeta_{kl} \rangle = \frac{s_2}{15} (\delta_{ij} \delta_{kl} + \delta_{ik} \delta_{jl} + \delta_{il} \delta_{jk}). \quad (\text{C11})$$

The full covariance matrix M is 11-dimensional. Fortunately from Eq. C2-C11, we see that M is block diagonal and the part of M due to $\zeta_{12}, \zeta_{23}, \zeta_{13}, \eta_1, \eta_2$, and η_3 is simply

$$M_2 = \text{Diag} \left(\frac{s_2}{15}, \frac{s_2}{15}, \frac{s_2}{15}, \frac{s_1}{3}, \frac{s_1}{3}, \frac{s_1}{3} \right). \quad (\text{C12})$$

The Gaussian distribution

$$p_G(V_1, \dots, V_{11}) \prod_i dV_i = \frac{1}{\sqrt{(2\pi)^{11} \det M}} \exp \left(-\frac{1}{2} \mathbf{V}^T M^{-1} \mathbf{V} \right) \prod_i dV_i \quad (\text{C13})$$

is invariant under coordinate transformation, and so we can evaluate it in any convenient coordinate system. Following [5], we can define the variables

$$\sigma_2 x = -(\zeta_{11} + \zeta_{22} + \zeta_{33}), \quad (\text{C14})$$

$$\sigma_2 y = -\frac{1}{2}(\zeta_{11} - \zeta_{33}), \quad (\text{C15})$$

$$\sigma_2 z = -\frac{1}{2}(\zeta_{11} - 2\zeta_{22} + \zeta_{33}). \quad (\text{C16})$$

to diagonalize the correlations between the diagonal elements of ζ_{ij} . In place of δ and μ , we will also use the normalized variables

$$\nu = \frac{\delta}{\sigma_0}, \quad (\text{C17})$$

$$u = \frac{\mu}{\sigma_\mu}. \quad (\text{C18})$$

The part of M related to ν, u, x, y , and z can then be written as

$$M_1 = \begin{pmatrix} 1 & \alpha & \gamma & 0 & 0 \\ \alpha & 1 & \beta & 0 & 0 \\ \gamma & \beta & 1 & 0 & 0 \\ 0 & 0 & 0 & \frac{1}{15} & 0 \\ 0 & 0 & 0 & 0 & \frac{1}{5} \end{pmatrix}, \quad (\text{C19})$$

with α and β denote

$$\alpha = \frac{1}{2\sigma_0\sigma_\mu}, \quad (\text{C20})$$

$$\beta = \frac{1}{2\sigma_2\sigma_\mu} \frac{ds_1}{ds_0}, \quad (\text{C21})$$

$$\gamma = \frac{s_1}{\sigma_0\sigma_2}. \quad (\text{C22})$$

and hence α is reduced to γ and β becomes 1. Therefore u and x are perfectly correlated. In this case the joint probability distribution is reduced to [11, 12]

$$P_G(\nu, u, x, y, z) = P_G(\nu, x, y, z) \delta_D(x - u). \quad (\text{C25})$$

If the window function is Gaussian, then

$$\frac{ds_1}{ds_0} = \frac{s_2}{s_1}, \quad (\text{C23})$$

$$\sigma_\mu^2 = \frac{s_2}{4s_1^2}, \quad (\text{C24})$$

However, we will not assume Gaussian window here. In this case, p_G is given by

$$p_G(\nu, u, \zeta_i, \vec{\eta}) \prod dV_i = \frac{1}{\sqrt{(2\pi)^{11} \det M}} e^{-Q} d\nu du d^3\eta \prod_{i=1}^6 d\zeta_i. \quad (\text{C26})$$

We have denoted ζ_{ii} by ζ_i for $i = 1, 2$, and 3 , while ζ_{12} , ζ_{23} and ζ_{31} by ζ_4 , ζ_5 , and ζ_6 respectively. Using Eq. C19 and C12, the quadratic form Q can be expressed as

$$\begin{aligned} Q &= \frac{1}{2} \mathbf{V}^T M^{-1} \mathbf{V} \\ &= \frac{1}{2(1 - \alpha^2 - \beta^2 + \alpha\beta\gamma)} \left[u^2 + (1 - \alpha^2)x^2 + (1 - \beta^2)\nu^2 - (\gamma - 2\alpha\beta)x\nu - (2\beta - \alpha\gamma)ux - (2\alpha - \beta\gamma)u\nu \right] \\ &\quad + \frac{15}{2}y^2 + \frac{5}{2}z^2 + \frac{15}{2s_2}(\zeta_4^2 + \zeta_5^2 + \zeta_6^2) + \frac{3}{2s_1}\vec{\eta} \cdot \vec{\eta}. \end{aligned} \quad (\text{C27})$$

The volume element for a 3×3 symmetric matrix can be written in term of the eigenvalues in the principle frame [5]

$$\prod_{i=1}^6 d\zeta_i = |(\lambda_1 - \lambda_2)(\lambda_2 - \lambda_3)(\lambda_3 - \lambda_1)| d\lambda_1 d\lambda_2 d\lambda_3 dV(SO(3)), \quad (\text{C28})$$

where λ_i is the eigenvalue in the principle frame and we assume that the eigenvalues are ordered such that

$$\lambda_1 \geq \lambda_2 \geq \lambda_3. \quad (\text{C29})$$

In the principle frame, x , y and z are defined by Eq. C14-C16 with ζ_{ii} replaced by λ_i . $dV(SO(3))$ is the volume elements of the $SO(3)$ group. The probability distribution is independent of it. We will integrate over it and we will get a factor of $2\pi^2$.

Using Eq. C28 and C14-C16, we get

$$d\nu du d^3\eta \prod_{i=1}^6 d\zeta_i \frac{1}{\sqrt{\det M}} = d\nu du d^3\eta 2\sigma_2^3 |y(z^2 - y^2)| dx dy dz \frac{1}{\sqrt{\det M_1 \det M_2}}. \quad (\text{C30})$$

Note that the Jacobian determinant $|\partial(\lambda_1, \lambda_2, \lambda_3)/\partial(x, y, z)|$ from the measure and $\det M$ cancels each other. From Eq. C19 and C12, we have

$$\det M_1 \det M_2 = \frac{(1 - \alpha^2 - \beta^2 + \alpha\beta\gamma)s_1^3 s_2^3}{9 \times 15^5}. \quad (\text{C31})$$

and hence

$$d\nu du d^3\eta \int_{S_3} \prod_{i=1}^6 d\zeta_i \frac{1}{(2\pi)^{11/2} \sqrt{\det M}} = \frac{3 \times 15^{5/2}}{(2\pi)^{7/2} \sqrt{1 - \alpha^2 - \beta^2 + \alpha\beta\gamma}} |y(z^2 - y^2)| d\nu du dx dy dz \frac{d^3\eta}{\sigma_1^3}. \quad (\text{C32})$$

The number density of peaks can be obtained by the Kac-Rice formula [5]

$$\begin{aligned} n_{\text{pk}}(\mathbf{r}) &= |\det \zeta_{ij}| \Theta(\lambda_3) \delta_{\text{D}}(\vec{\eta}(\mathbf{r})) \\ &= \frac{\sigma_2^3}{3^3} |(2z - x)[(z + x)^2 - (3y)^2]| \Theta(\lambda_3) \delta_{\text{D}}(\vec{\eta}(\mathbf{r})), \end{aligned} \quad (\text{C33})$$

where the constraint $\delta_{\text{D}}(\vec{\eta}(\mathbf{r}))$ selects the extremum points and $\lambda_3 > 0$ ensures that the extrema are peaks.

We can obtain the mean differential number density by averaging over the joint Gaussian distribution as

$$\begin{aligned} \mathcal{N}_{\text{pk}}(\nu, u, x, y, z) d\nu du dx dy dz \\ &= d\nu du |2\sigma_2^3 y(z^2 - y^2)| dx dy dz \int d^3\eta P_{\text{G}}(\nu, u, x, y, z, \vec{\eta}) \frac{\sigma_2^3}{3^3} |(2z - x)[(z + x)^2 - (3y)^2]| \Theta(\lambda_3) \delta_{\text{D}}(\vec{\eta}) \\ &= \frac{5^{5/2} \sqrt{3}}{(2\pi)^{7/2} \sqrt{1 - \alpha^2 - \beta^2 + \alpha\beta\gamma}} \frac{\sigma_2^3}{\sigma_1^3} |y(z^2 - y^2)(2z - x)[(z + x)^2 - (3y)^2]| e^{-\tilde{Q}} \chi d\nu du dx dy dz, \end{aligned} \quad (\text{C34})$$

where χ is the indicator function, which is 1 when the integration variables are in the specified domain, zero otherwise and \tilde{Q} denotes

$$\begin{aligned} \tilde{Q} &= \frac{1}{2} \mathbf{x}^T M^{-1} \mathbf{x} \\ &= \frac{1}{2(1 - \alpha^2 - \beta^2 + \alpha\beta\gamma)} \left[u^2 + (1 - \alpha^2)x^2 + (1 - \beta^2)\nu^2 - (\gamma - 2\alpha\beta)x\nu - (2\beta - \alpha\gamma)ux - (2\alpha - \beta\gamma)u\nu \right] \\ &\quad + \frac{15}{2}y^2 + \frac{5}{2}z^2. \end{aligned} \quad (\text{C35})$$

The ESP number density can be obtained by imposing the first-crossing constraint on the peak number density as [4, 11, 12]

$$\begin{aligned} \mathcal{N}_{\text{esp}}(s_0, u, x, y, z) \Delta s_0 du dx dy dz \\ &= \frac{5^{5/2} \sqrt{3}}{(2\pi)^{7/2} \sqrt{1 - \alpha^2 - \beta^2 + \alpha\beta\gamma}} \frac{\sigma_2^3}{\sigma_1^3} du dx dy dz \int_{\nu_c}^{\nu_c + \mu \frac{\Delta s_0}{\sigma_0}} d\nu |y(z^2 - y^2)(2z - x)[(z + x)^2 - (3y)^2]| e^{-\tilde{Q}} \chi. \end{aligned} \quad (\text{C36})$$

It essentially ensures that the smoothed δ upcrosses the barrier by the condition that

$$\delta(s) > \delta_c, \quad \delta(s - \Delta s) < \delta_c, \quad (\text{C37})$$

which translates to

$$\delta_c < \delta(s) < \delta_c + \mu \Delta s. \quad (\text{C38})$$

The upcrossing condition also requires μ to be positive.

For small Δs_0 , we can reduce the ν -integral to

$$\begin{aligned} \mathcal{N}_{\text{esp}}(s_0, u, x, y, z) \Delta s_0 du dx dy dz \\ &= \frac{5^{5/2} \sqrt{3}}{(2\pi)^{7/2} \sqrt{1 - \alpha^2 - \beta^2 + \alpha\beta\gamma}} \frac{\sigma_2^3}{\sigma_1^3} \frac{\sigma_\mu \Delta s_0}{\sigma_0} du dx dy dz u |y(z^2 - y^2)(2z - x)[(z + x)^2 - (3y)^2]| e^{-\tilde{Q}(\nu_c)} \chi. \end{aligned} \quad (\text{C39})$$

Note that \tilde{Q} now is evaluated at $\nu = \nu_c$.

As u only couples to x and ν_c , we can integrate over z and y as in [5]. The ESP number density in the interval Δs_0 is given by

$$\mathcal{N}_{\text{esp}}(s_0) \Delta s_0 = \frac{1}{(2\pi)^2} \left(\frac{\sigma_2}{\sqrt{3}\sigma_1} \right)^3 \frac{\sigma_\mu \Delta s_0}{\sigma_0} e^{-\frac{\nu_c^2}{2}} E(\nu_c, \alpha, \beta, \gamma), \quad (\text{C40})$$

where E is defined as

$$E(\nu, \alpha, \beta, \gamma) = \int_0^\infty dx \int_0^\infty du u f(x) \frac{1}{\sqrt{(2\pi)^2 (1 - \alpha^2 - \beta^2 + \alpha\beta\gamma)}} e^{-B}, \quad (\text{C41})$$

with B given by

$$B(\nu, x, u; \alpha, \beta, \gamma) = \frac{1}{2(1 - \alpha^2 - \beta^2 + \alpha\beta\gamma)} \left[\alpha(\alpha - \beta\gamma)\nu^2 + u^2 + (1 - \alpha^2)x^2 - (\gamma - 2\alpha\beta)x\nu - (2\beta - \alpha\gamma)ux - (2\alpha - \beta\gamma)u\nu \right]. \quad (\text{C42})$$

The function $f(x)$ is given by [5]

$$f(x) = \frac{x^3 - 3x}{2} \left\{ \text{erf} \left[\sqrt{\frac{5}{2}} x \right] + \text{erf} \left[\sqrt{\frac{5}{2}} \frac{x}{2} \right] \right\} + \sqrt{\frac{2}{5\pi}} \left[\left(\frac{31x^2}{4} + \frac{8}{5} \right) e^{-\frac{5x^2}{8}} + \left(\frac{x^2}{2} - \frac{8}{5} \right) e^{-\frac{5x^2}{4}} \right]. \quad (\text{C43})$$

Using $\nu\mathcal{N}(\nu) = 2s\mathcal{N}(s)$, we arrive at

$$\mathcal{N}_{\text{esp}}(\nu_c) = \frac{1}{(2\pi)^2} \left(\frac{\sigma_2}{\sqrt{3}\sigma_1} \right)^3 \frac{1}{\nu_c\alpha} e^{-\frac{\nu_c^2}{2}} E(\nu_c, \alpha, \beta, \gamma). \quad (\text{C44})$$

Therefore f_{esp} is given by

$$f_{\text{esp}}(\nu_c) = \frac{M}{\rho_m} \mathcal{N}_{\text{esp}}(\nu_c) = \frac{V}{V_*} \frac{e^{-\frac{\nu_c^2}{2}}}{\sqrt{2\pi}} \frac{1}{\nu_c\alpha} E(\nu_c, \alpha, \beta, \gamma). \quad (\text{C45})$$

To facilitate the comparison with [12], we have defined two volumes

$$V = \frac{M}{\rho_m}, \quad V_* = (6\pi)^{\frac{3}{2}} \left(\frac{\sigma_1}{\sigma_2} \right)^3. \quad (\text{C46})$$

When Gaussian window is used, α reduces to γ , and hence the prefactor is the same as that in [12], and E can be regarded as a generalization of G_1 in [12].

Now we further generalize the ESP mass function to the moving barrier case. The first crossing condition is modified to

$$\delta(s) > B(s), \quad \delta(s - \Delta s) < B(s - \Delta s), \quad (\text{C47})$$

which means

$$B(s) < \delta(s) < B(s) + [\mu - B'(s)]\Delta s. \quad (\text{C48})$$

To upcross the barrier, the minimal u is modified to

$$u_0 = \frac{B'(s)}{\sigma_\mu}. \quad (\text{C49})$$

This effectively modifies the integration limits of ν and u integrals, and the end results is that E -integral is modified to

$$E(\nu, \alpha, \beta, \gamma) = \int_0^\infty dx f(x) \int_{u_0}^\infty du (u - u_0) \frac{e^{-B}}{\sqrt{(2\pi)^2(1 - \alpha^2 - \beta^2 + \alpha\beta\gamma)}}. \quad (\text{C50})$$

Appendix D: Relation to spherical collapse

Conceptually, going beyond the tophat shape is subtle. This is because the window function plays two roles. In theory calculations, it smooths the initial overdensity field. In the other, which is close to the way measurements are made, it is a weighting function which selects a fraction of the local dark matter particles that go on

to become members of the Eulerian halo later on. For a tophat, these two roles appear to be the same, but for other filters, they need not be. We discuss this below.

The main text showed that the Lagrangian protohalo profile is more extended than a tophat. There, the profile was obtained using the particle distribution. Therefore, it is tempting to associate it with a density profile, and hence to ask how well the spherical evolution model describes its evolution. Our main goal is to show that, in

this respect, it really is better to think of this profile as a smoothing window, W_{eff} , and not as a profile.

Specifically, it is tempting to define the mean overdensity inside r as

$$\bar{\eta}(\leq r) = \frac{3 \int_0^r dr' r'^2 n_h(r')}{r^3 \bar{n}_m} - 1. \quad (\text{D1})$$

However, since $n_h = p_h \bar{n}_m$ and $p_h \leq 1$, the quantity above is guaranteed to be negative. Therefore, if we were to use this $\bar{\eta}$ as a proxy for overdensity in the spherical evolution model, we would conclude that the protohalo patch would not shrink and collapse (in comoving coordinates). This is the wrong answer, of course, since the particles were identified precisely because they did form a collapsed object.

The error arises because the argument above does not account for the fact that the particles coming from further away must have had higher infall velocities, and the naive application of the spherical model argument has ignored this. It is straightforward to include the fact that the initial velocities are perturbed from the initial Hubble flow in the spherical model analysis. But instead of doing so directly, we think the discussion which follows makes a similar point.

First, define

$$\bar{\delta}_{\text{Lag}} = \int d\mathbf{x}' \delta_m(\mathbf{x}') W_{\text{eff}}(\mathbf{x}'). \quad (\text{D2})$$

This expression represents a smoothing of the initial overdensity fluctuation field centered on the origin (in this case, the center of the protohalo patch). However, the continuity equation relates the overdensity to the divergence of the velocities: so the average over δ_m above is like averaging over the velocity divergence. It is this smoothed overdensity which should be inserted into the spherical evolution model. In this respect, $W_{\text{eff}} \leq 1$ in the expression above is a simple way to account for the fact that some particles fall onto the protohalo center and others escape; i.e., it is the motions, the displacements from the initial positions, which matter. The role of W_{eff} is to only count those particles in the initial conditions whose displacements will bring them into the final collapsed object. Previous work has shown that $\bar{\delta}_{\text{Lag}} \geq \delta_c$ when a tophat smoothing window is used [22, 39], so it should be no surprise that it is also larger than δ_c when W_{eff} is used. This shows explicitly why W_{eff} can be thought of as playing two distinct roles: it is both a fraction of particles, and a smoothing filter which should be applied to the Lagrangian overdensity fluctuation field.

-
- [1] W. H. Press and P. Schechter, *ApJ* **187**, 425 (1974).
 - [2] R. K. Sheth and G. Tormen, *MNRAS* **308**, 119 (1999).
 - [3] J. R. Bond, S. Cole, G. Efstathiou, and N. Kaiser, *ApJ* **379**, 440 (1991).
 - [4] M. Musso and R. K. Sheth, *MNRAS* **423**, 102 (2012).
 - [5] J. M. Bardeen, J. R. Bond, N. Kaiser, and A. S. Szalay, *ApJ* **304**, 15 (1986).
 - [6] J. R. Bond and S. T. Myers, *ApJS* **103**, 1 (1996).
 - [7] V. Desjacques, *Phys. Rev. D* **78**, 103503 (2008), arXiv:0806.0007.
 - [8] V. Desjacques and R. K. Sheth, *Phys. Rev. D* **81**, 023526 (2010), arXiv:0909.4544.
 - [9] V. Desjacques, M. Crocce, R. Scoccimarro, and R. K. Sheth, *Phys. Rev. D* **82**, 103529 (2010), arXiv:1009.3449.
 - [10] V. Desjacques, *Phys. Rev. D* **87**, 043505 (2012), arXiv:1211.4128.
 - [11] L. Appel and B. J. T. Jones, *MNRAS* **245**, 522 (1990).
 - [12] A. Paranjape and R. K. Sheth, *MNRAS* **426**, 2789 (2012).
 - [13] A. Paranjape, R. K. Sheth, and V. Desjacques, *MNRAS* **431**, 1503 (2013), arXiv:1210.1483.
 - [14] M. Biagetti, K. C. Chan, V. Desjacques, and A. Paranjape, *MNRAS* **441**, 1457 (2014).
 - [15] J. E. Gunn and J. R. Gott, III, *ApJ* **176**, 1 (1972).
 - [16] P. J. E. Peebles, *The Large-Scale Structure of the Universe* (Princeton University Press, New Jersey, 1980).
 - [17] T. Padmanabhan, *Structure formation in the Universe* (Cambridge University Press, Cambridge, 1993).
 - [18] D. Lynden-Bell, *MNRAS* **136**, 101 (1967).
 - [19] C. Porciani, A. Dekel, and Y. Hoffman, *MNRAS* **332**, 339 (2002).
 - [20] N. Dalal, M. White, J. R. Bond, and A. Shirokov, *ApJ* **687**, 12 (2008).
 - [21] A. Elia, A. D. Ludlow, and C. Porciani, *MNRAS* **421**, 3472 (2012).
 - [22] G. Despali, G. Tormen, and R. K. Sheth, *MNRAS* **431**, 1143 (2013).
 - [23] T. Baldauf, in *Perturbative approaches to redshift space distortions workshop, Zurich* (2012).
 - [24] T. Baldauf, V. Desjacques, and U. Seljak (2014), arXiv:1405.5885.
 - [25] K. C. Chan (2015), arXiv:1507.04753.
 - [26] A. Paranjape, E. Sefusatti, K. C. Chan, V. Desjacques, P. Monaco, and R. K. Sheth, *MNRAS* **436**, 449 (2013).
 - [27] M. Musso, A. Paranjape, and R. K. Sheth, *MNRAS* **427**, 3145 (2012).
 - [28] U. Seljak and M. Zaldarriaga, *ApJ* **469**, 437 (1996), arXiv:astro-ph/9603033.
 - [29] M. Crocce, S. Pueblas, and R. Scoccimarro, *MNRAS* **373**, 369 (2006), arXiv:astro-ph/0606505.
 - [30] V. Springel, *MNRAS* **364**, 1105 (2005), arXiv:astro-ph/0505010.
 - [31] M. Davis, G. Efstathiou, C. S. Frenk, and S. D. M. White, *ApJ* **292**, 371 (1985).
 - [32] G. Despali and *et al.*, in preparation (2015).
 - [33] N. Frusciante and R. K. Sheth, *JCAP* **1211**, 016 (2012), arXiv:1208.0229.
 - [34] K. C. Chan, R. Scoccimarro, and R. K. Sheth, *Phys. Rev.*

- D **85**, 083509 (2012), arXiv:1201.3614.
- [35] K. C. Chan, R. K. Sheth, and R. Scoccimarro, in preparation (2015).
- [36] B. E. Robertson, A. V. Kravtsov, J. Tinker, and A. R. Zentner, *ApJ* **696**, 636 (2009).
- [37] A. D. Ludlow and C. Porciani, *MNRAS* **413**, 1961 (2011), arXiv:1011.2493.
- [38] O. Hahn and A. Paranjape, *MNRAS* **438**, 878 (2014).
- [39] R. K. Sheth, H. J. Mo, and G. Tormen, *MNRAS* **323**, 1 (2001).